

Remotely controlled nanofluidic implantable platform for tunable drug delivery

*Original*

Remotely controlled nanofluidic implantable platform for tunable drug delivery / Di Trani, Nicola; Silvestri, Antonia; Bruno, Giacomo; Geninatti, Thomas; Ying Xuan Chua, Corrine; Gilbert, April; Rizzo, Giulia; Filgueira, Carly S.; Demarchi, Danilo; Grattoni, Alessandro. - In: LAB ON A CHIP. - ISSN 1473-0197. - ELETTRONICO. - (2019). [10.1039/c9lc00394k]

*Availability:*

This version is available at: 11583/2736885 since: 2019-07-11T20:00:25Z

*Publisher:*

Royal Society of Chemistry

*Published*

DOI:10.1039/c9lc00394k

*Terms of use:*

This article is made available under terms and conditions as specified in the corresponding bibliographic description in the repository

*Publisher copyright*

(Article begins on next page)

# Lab on a Chip

Accepted Manuscript



This article can be cited before page numbers have been issued, to do this please use: N. Di Trani, A. Silvestri, G. Bruno, T. Geninatti, C. Y. X. Chua, A. Gilbert, G. Rizzo, C. S. Filgueira, D. Demarchi and A. Grattoni, *Lab Chip*, 2019, DOI: 10.1039/C9LC00394K.



This is an Accepted Manuscript, which has been through the Royal Society of Chemistry peer review process and has been accepted for publication.

Accepted Manuscripts are published online shortly after acceptance, before technical editing, formatting and proof reading. Using this free service, authors can make their results available to the community, in citable form, before we publish the edited article. We will replace this Accepted Manuscript with the edited and formatted Advance Article as soon as it is available.

You can find more information about Accepted Manuscripts in the [author guidelines](#).

Please note that technical editing may introduce minor changes to the text and/or graphics, which may alter content. The journal's standard [Terms & Conditions](#) and the ethical guidelines, outlined in our [author and reviewer resource centre](#), still apply. In no event shall the Royal Society of Chemistry be held responsible for any errors or omissions in this Accepted Manuscript or any consequences arising from the use of any information it contains.

# Remotely controlled nanofluidic implantable platform for tunable drug delivery

Nicola Di Trani<sup>1,2</sup>, Antonia Silvestri<sup>1,3</sup>, Giacomo Bruno<sup>1,3</sup>, Thomas Geninatti<sup>1</sup>, Corrine Ying Xuan Chua<sup>1</sup>, April Gilbert<sup>1</sup>, Giulia Rizzo<sup>1,3</sup>, Carly S. Filgueira<sup>1</sup>, Danilo Demarchi<sup>3</sup>, Alessandro Grattoni<sup>1,4,5\*</sup>

<sup>1</sup>Nanomedicine Department, Houston Methodist Research Institute, Houston, TX, USA.

<sup>2</sup>University of Chinese Academy of Science (UCAS), Shijingshan, 19 Yuquan Road, Beijing 100049, China

<sup>3</sup>Department of Electronics and Telecommunications, Politecnico di Torino, Turin 10024, Italy

<sup>4</sup>Department of Surgery, Houston Methodist Hospital, 6550 Fannin Street, Houston, TX, 77030, USA.

<sup>5</sup>Department of Radiation Oncology, Houston Methodist Hospital, 6550 Fannin Street, Houston, TX, 77030, USA.

\*Corresponding Author, agrattoni@houstonmethodist.org, phone: +1 (713) 441-7324

**Keywords:** drug delivery, nanofluidics, remote control, implant, blue tooth communication.

## Abstract

Chronic diseases such as hypertension and rheumatoid arthritis are persistent ailments that require personalized lifelong therapeutic management. However, the difficulty of adherence to strict dosing schedule compromises therapeutic efficacy and safety. Moreover, the conventional one-size-fits-all treatment approach is increasingly challenged due to the intricacies of inter- and intra-individual variability. While accelerated technological advances have led to sophisticated implantable drug delivery devices, flexibility in dosage and timing modulation to tailor precise treatment to individual needs remains an elusive goal. Here we describe the development of a subcutaneously implantable remote-controlled nanofluidic device capable of sustained drug release with adjustable dosing and timing. By leveraging a low intensity electric field to modify concentration driven diffusion across a nanofluidic membrane, the rate of drug administration can be increased, decreased or stopped via Bluetooth remote command. We demonstrate in vitro the release modulation of enalapril and methotrexate, first-line therapeutics for treatment of hypertension and rheumatoid arthritis, respectively. Further, we show reliable remote communication and device biocompatibility via in vivo studies. Unlike pulsatile release regimen typical of some conventional controlled delivery systems, our implant offers a continuous drug administration that avoids abrupt fluctuations, which could affect response and tolerability. Our system could set the foundation for an on-demand delivery platform technology for long term management of chronic diseases.

## Introduction

The escalating burden of chronic diseases constitutes a major public health problem, accounting for approximately two-thirds of all deaths and 75% of healthcare expenditures<sup>1,2</sup>. With a protracted course of disease and requirement for continuous therapeutic management, chronic conditions constitute a complex, long-term challenge for patients and healthcare system alike. Moreover, healthcare systems are typically focused on acute episodic care rather than structured continuous management of the disease, which increases the economic burden<sup>3</sup>. Most chronic diseases such as hypertension are often accompanied by various comorbidities, thus requiring attentive vigilance in disease management, specifically compliance to therapeutic interventions. However, only approximately 50% of individuals with chronic diseases adhere to treatment regimen, posing significant risks of complications and even mortality<sup>4</sup>. While the advent of implantable sustained release platforms<sup>5,6</sup> have significantly improved treatment regimen of certain pathologies, not all chronic diseases benefit from constant drug administration. Considering that physiologic variables such as blood pressure are typically predictably synchronized with circadian activity<sup>7</sup>, the conventional paradigm of constant drug delivery to target these parameters is unnecessary and often associated with undesirable problems of resistance, tolerability and side effects<sup>8</sup>. For instance, anti-inflammatory drugs for rheumatoid arthritis are most beneficial during the 4-5 hour window of night-time immune hyperactivity, rendering daylong systemic immunosuppression needless and unwarranted<sup>9,10</sup>. More importantly, advances in precision medicine has challenged the conventional one-size-fits-all blanket treatment approach due to the intricacies of inter- and intra-individual variability. This motivated the need for technological innovations in drug delivery that meet the demand for customizable therapy to achieve maximal treatment efficacy with minimal side effects.

Thus far, implantable delivery systems that provide drug administration at a defined time, and dose or rate, constitute a desirable but unmet clinical need. Recent advances have led to developments of such technologies, some of which include polymeric, pump, and microelectromechanical-based systems (MEMS) for either pulsatile or continuous release<sup>11,12</sup>. Biodegradable polymeric systems<sup>13,14</sup> allow for multiple-pulse drug release, whereas propellant infusion pumps<sup>15</sup> offer a steady release over time; however both lack of dosing control after implantation. While peristaltic implantable pumps such as SynchroMed Medtronic<sup>16,17</sup> offer zero-order release manner with externally modifiable dosing, these benefits could be overlooked due to prohibitive costs and bulky sizes. Research efforts have also focused on trigger-dependent systems based on reservoirs covered by membranes with tunable permeability to activate

modulated drug release in a burst manner<sup>18,19</sup>. However, a point of consideration for feasibility and convenience of implementation is that these devices usually require external stimuli such as electromagnetic fields or near-infrared light throughout the duration of the release. As such, this could be cumbersome considering individuals would need to be subjected to the stimuli for long periods of time, not to mention the possibility of injury due to repeated exposure to stimuli (i.e., thermal injury)<sup>18</sup>. Another development of note is using remote communication to control drug release, as represented by MEMS-based implants such as Microchip<sup>20</sup> and ChipRx<sup>21</sup>. Microchip is a silicon chip with twenty 600 nanoliter drug reservoirs that are individually opened via a wireless command. This system completed the first clinical trial in Europe for assessing the efficacy in treating women with osteoporosis (EudraCT, number 2010-020040-35)<sup>22</sup>. Albeit promising, limitations in reservoir size and quantity present challenges for long-term disease management. ChipRx (Lexington, KY, USA) uses a single electronic signal to open micrometric-sized holes to release drug. However, development was suspended due to undisclosed reasons. Moreover, it is important to note that pulsatile release systems such as the aforementioned MEMS-based implants causes abrupt fluctuations of drug concentrations, which may affect clinical response and tolerability<sup>23</sup>.

That said, an ideal programmable delivery system should entail: 1) zero-order release kinetics, 2) modulation capabilities for dosing-on-demand, tunable dose, rate and time, 3) wireless or remote communication capabilities for convenience of monitoring or telemedicine intents, 4) release stoppage when not needed (i.e., hypertension drug release only during sleep cycle) or when unexpected side effects occur, and 5) compact size dimension for feasibility of discrete implantation. With this mind, we developed a subcutaneously implantable delivery device for dosing modulation via remotely controlled application of a low-intensity electric field across a nanofluidic membrane. With no application of an electric field, the implant releases drugs through diffusion, driven by a concentration gradient between the reservoir and subcutaneous space. Therefore zero-order passive release is achieved without the use of mechanical parts by tailoring of the size of channels to the size and properties of drug molecules (net charge, molecular weight, hydrophobicity). By applying a small electric field across the membrane via two platinum electrodes, ionic species are forced to redistribute or are electrophoretically driven across the nanoconfined space, thus effectively actively modulating drug release rate. As such, our implant offers a continuous drug administration for smooth transition between different release phases. This allows for avoidance of peak-to-trough plasma fluctuations that affect drug administration efficiency and potentially causes adverse effects<sup>24</sup>.

In this work, we first demonstrate drug modulation capability by leveraging electric field across a nanofluidic membrane through in vitro studies. Next, we incorporated this technology into a drug delivery implant and characterized its capacity for reliable Bluetooth communication and release rate modulation. Finally, we validated telemetric capacity and biocompatibility of our remotely controlled drug delivery implant in rats and a non-human primate. Overall, we present the proof of concept of a telemetry-enabled delivery system, which could eventually allow physicians autonomy to access data, remotely adjust drug release and dosing schedule according to individual patients' needs. Our wirelessly programmable nanofluidic approach holds potential for the development of a drug delivery platform capable of maximizing therapeutic efficacy and minimizing side effects towards improving patient adherence, quality of life and treatment of chronic diseases.

## Materials and Methods

### Fabrication of silicon nanofluidic membrane

Silicon membranes were manufactured using standard semiconductor fabrication techniques described in detail elsewhere<sup>25</sup> (Figure 1A). Briefly, slit-nanochannels were obtained starting from a deposited silicon nitride (SiN) thin film (1.7  $\mu\text{m}$  thick) on a silicon (Si) wafer (700  $\mu\text{m}$  thickness). The inlet and outlet microchannels were perpendicularly etched on the silicon wafer with a cross-section of 1  $\mu\text{m}$   $\times$  3  $\mu\text{m}$  (Figure 1B). The nanochannels were obtained by removing a sacrificial tungsten layer, which lay between the Si and the SiN, with hydrogen peroxide ( $\text{H}_2\text{O}_2$ ) (Figure 1B, C). The configuration of slit-nanochannels parallel to the surface ensures high structural stability and mechanical robustness, while the addition of TaN/SiC layer coating to the membrane provides bioinertness<sup>26</sup>. This study utilized nanofluidic membranes of 13 nm and 200 nm, which features a geometrically organized array of 340,252 densely packed slit-nanochannels.

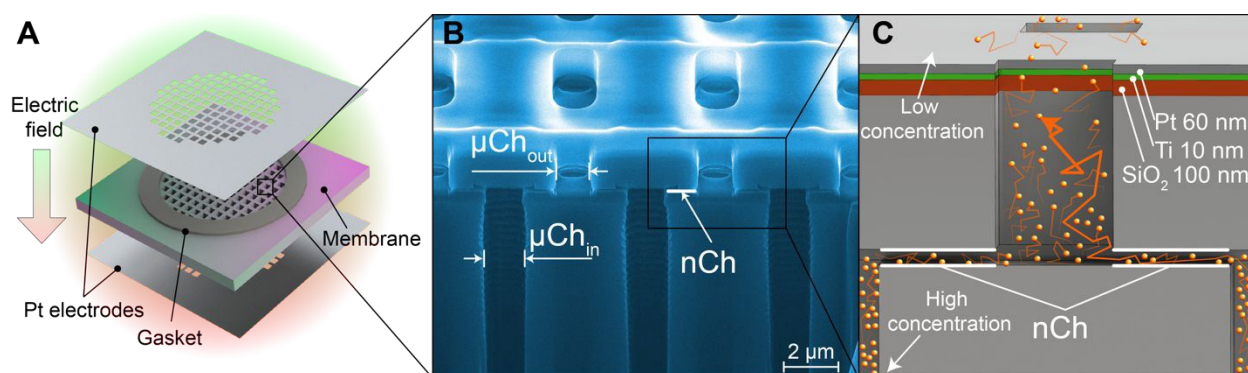


**Figure 1. Nanofluidic membrane and platinum electrodes. (A)** Schematic of nanofluidic membrane with Platinum (Pt) foil electrodes separated by gaskets. **(B)** FIB-SEM image of the nanofluidic membrane without electrodes. Inlet and outlet microchannels highlighted,  $\mu\text{Ch}_{\text{in}}$  and  $\mu\text{Ch}_{\text{out}}$  respectively. Nanochannels (nCh) are perpendicular to the  $\mu\text{Ch}$ . **(C)** Schematic of the deposited electrode stack achieved through the second method of electrode integration (sputtering). In order of deposition (bottom to top): silicon dioxide ( $\text{SiO}_2$ ; 100 nm, red layer), titanium (Ti; 10 nm, green layer), platinum (Pt; 60 nm, grey layer). Orange particles represent the diffusing drug molecules. Orange arrows represent the diffusing path.

### Incorporation of platinum electrodes on membrane

Platinum (Pt) electrodes were integrated on the silicon membrane using two different techniques, as previously described<sup>27</sup>. The first method uses 100  $\mu\text{m}$  thick Pt foils (Sigma Aldrich, St. Louis, MO, USA) which were laser cut (A-Laser, Inc., CA, USA) to fit the membrane in a 6 mm  $\times$  6 mm square shape and affixed to the membrane with UV Epoxy (OG116, Epoxy Technologies, Inc.). UV epoxy was cured overnight with a UV lamp (UVL-18, UVL) (Figure 1A). To prevent epoxy leakage into channels, a silicone gasket was positioned between the Pt foil on each side of the membrane (Figure 1A). The second method is a chemical vapor deposition (sputtering) of  $\text{SiO}_2$ -Ti-Pt stack on the top and bottom surface of the membrane (Figure 1C). First, the  $\text{SiO}_2$  (250 nm) substrate was deposited on the SiN surface, the presence of argon plasma ensured a defect-free dielectric layer. A Ti adhesion layer was deposited prior to the final Pt film. To avoid channel clogging and achieve equal layer thickness perpendicular to the membrane, Ti (10 nm) and Pt (60 nm) layers were deposited at a  $\sim 45^\circ$  angle with respect to the surface (Figure 1C). Insulated 36 AWG wires were connected to the electrodes with electrically conductive silver epoxy (H20E, Epoxy Technology, MA) and cured at 130  $^\circ\text{C}$  for 15 min. Pt foils were wired using a lead-free solder (SN99, MG Chemicals, BC, Canada). Additional details are available elsewhere<sup>27</sup>.

### Focused ion beam (FIB) – Scanning electron microscopy (SEM) imaging

Silicon nanofluidic membranes were evaluated using the Dual-Beam Ion-Beam (FIB) System FEI 235 at the Nanofabrication Facility of University of Houston, Texas. The membranes were imaged at an angle of  $52^\circ$  using the Scanning Electron Microscopy (SEM) in the FIB system.

### In vitro controlled release from membranes

Enalapril in vitro release test was performed with 13 nm nanochannels and Pt foils electrodes, while 200 nm membranes with sputtered electrodes were used for methotrexate. Membranes were first immersed in isopropyl alcohol to ensure proper nanochannel wetting, then rinsed in deionized (DI)  $\text{H}_2\text{O}$ , and inserted in a dual-reservoir diffusion apparatus<sup>28</sup>. The source chamber



contained either 200  $\mu\text{L}$  of 10 mg/mL enalapril (Cayman Chemical, Ann Arbor, MI) or 200  $\mu\text{L}$  of 3 mg/mL methotrexate in 50 mM NaCl. Both drugs are negatively charged,  $-1q$  ( $= -1.6 \times 10^{-19}$  C) for enalapril and  $-2q$  ( $= -3.2 \times 10^{-19}$  C) for methotrexate. UV-cuvettes loaded with 4.45 mL of 50 mM NaCl in DI  $\text{H}_2\text{O}$  were employed as a sink reservoirs. The assembled custom cuvette systems were loaded onto a robotic carousel<sup>29</sup> of a Cary 50 UV-vis spectrophotometer (Agilent Technologies). Electric potentials were applied to the membrane electrodes using a DC power supply (E3643A, Agilent Technologies) in three phases with the following sequence: 0 V, -1.5 V, 0 V, +1.5 V. Each phase was run for 8 hours for the methotrexate study and 24 hours for enalapril. UV absorption measurements of the sink solution were automatically performed by the robotic carousel every 7.5 minutes. Wavelengths used for detection were 287 nm for methotrexate and 219 nm for enalapril.

### Printed Circuit Board (PCB) and remote communications

The printed circuit board (PCB) was designed for the control of therapeutic release. The System-on-Chip (SoC) CC2541 (Texas Instrument) was used for the Bluetooth Low Energy (BLE) communication since it provides ultra-low energy consumption. A commercially available discoidal CR2016 (VARTA) battery was used as a power supply for the board. The battery has a total capacity of 90 mAh. A step-down voltage converter (LM3670, Texas Instrument) was used to lower the battery voltage from 3 V to 1.5 V. Two of the available general-purpose input-output (GPIO) pins (P1 and P2) were connected to the electrodes used for drug modulation. P1 was connected to the converter for the 1.5 V output, while P2 was connected directly to the GPIO for 3V. The wireless communication with a remote PC was implemented through a USB Bluetooth Dongle CC2540 (Texas Instrument) and MATLAB® script.

### Power consumption evaluation

The power consumption of the PCB was evaluated considering the instant current absorbed by the PCB. An oscilloscope (U2702A, Agilent Technologies) was used to monitor the voltage across a resistor of 50 $\Omega$ , emulating the internal load of the battery. Power supply (3 V) was provided by a power generator (E3643A, Agilent Technologies).

### Implant assembly

The implant capsule made of polyether ether ketone (PEEK) was machined at the machine shop core of the Houston Methodist Hospital. The capsule hosts two separate compartments: one for the membrane that also serves as a drug reservoir and the other for the battery and electronics.



The reservoir was sealed with a PEEK lid where two loading/venting ports were incorporated. Ports were sealed with implantable self-sealing silicone glue (Nusil MED3-4213, Nusil Technology). Biocompatible thermal epoxy (Epotek 302-3M, Epoxy Technology) was centrifuged at 5000 x g for 2 minutes to remove bubbles. Battery and electronics were embedded in the implant capsule with thermal epoxy under a sterile laminar flow hood and cured in a sterile container at 65°C for 3 hours. The membrane was glued in place with biocompatible UV epoxy (OG116, Epoxy Technologies, Inc.) and cured overnight with a UV lamp (UVL-18, UVL). Finally, the lid was sealed with UV epoxy.

### **Implant leakage test**

Assembled implants (n=6) were loaded through the loading ports with 550 µL of 1 mg/mL rhodamine B (Sigma) in PBS using two 3 mL syringes with 25G needles, one for loading and the other for venting. The silicone loading ports were then sealed with UV epoxy to avoid any leakage. The implants were placed in a borosilicate bottle containing 20 mL of PBS and kept in a 37°C incubator under constant agitation to ensure sample homogeneity for the 12-day duration of the experiment. Samples of 200 µL were collected daily and replaced with fresh PBS solution. Sample concentration was analyzed with a high precision spectrofluorimeter (PC1, ISS) using excitation wavelength 525 nm and emission of 550 nm.

### **In vitro communication stability**

Connection between the assembled implants (n=5) and the computer was performed at increasing distances from 30 cm to 180 cm. We measured the received signal strength indication (RSSI) as a measure a communication quality. Communication was performed in two conditions, with the implants in air or submerged in water as a surrogate for the subcutaneous implantation. The communication test was performed over 60 min and repeated three times for each circuit.

### **In vitro drug release from assembled implants**

A customized cuvette was used for the release study, specifically designed to host the implant for measurement in the UV-Vis spectrophotometer carousel. The body of the cuvette is composed of two parts: a cuvette and a PEEK container to host the implant glued together with UV epoxy (OG116, Epoxy Technologies, Inc.). 13 nm nanochannel membrane with sputtered electrodes was embedded in the implant. The implant reservoir was filled with 550 µL of methotrexate (500 µg/mL in 50 mM NaCl). The sink solution of 7 mL 50 mM NaCl was under continuous agitation via magnetic stirring to ensure sample homogeneity. Under our experimental condition (pH 7),

methotrexate has a net charge of  $-2q$ . Drug concentration measurement in the sink solution was performed every 7.5 minutes via UV-Vis spectroscopy at a wavelength of 287 nm. In the first 60 hours, no voltage (0 V) was applied to the electrodes, followed by a voltage of +1.5V applied for 9h, and then 0V for 14h and +1.5V for 25h. The total duration of the experiment was 100 h.

### **In vivo biocompatibility and communication testing in rats**

10 week-old male Wistar-Kyoto rats ( $n=6$ ) from Charles River Laboratories (Wilmington, MA) were used in this study. Animals were housed at the Houston Methodist Research Institute (HMRI) Comparative Medicine animal facility in standard cages. All animal experiments conducted were approved by the Institutional Animal Care and Use Committee (IACUC) of HMRI and performed in accordance with the Animal Welfare Act and the NIH Guide for the Care and Use of Laboratory Animals. Each implant was assembled as previously described, and reservoir loaded with sterile PBS. Using aseptic technique, a 2 cm incision was made on the dorsum of the animal. The implant was positioned in a subcutaneous pocket with circuitry facing the epidermis and membrane facing the dermis. The incision was closed with metal wound clips. Bluetooth communication with the implanted implant was performed every 5 minutes using the MATLAB® script running on a computer positioned 2 meters away from the animal. Connections to the implant were performed at regular intervals of 24 h for the whole duration of the experiment. The applied phases were: passive, active (1.5 V), passive, active (-1.5 V), each for 5 days. Communication reliability was assessed by quantifying the number of advertisement packets that were lost during the discovery routine of the MATLAB® script running on the computer resulting in a non-successful discovery of the implant. After 21 days, the animals were euthanized and implants explanted for analysis.

### **In vivo biocompatibility and communication testing in non-human primate (NHP)**

A 4 year-old rhesus macaque (*Macaca mulatta*) was used in a non-terminal study setting, to assess the biocompatibility and communication performances in a most relevant animal model in view of potential clinical translation. The NHP experiments were conducted at the AAALAC-I accredited Michale E. Keeling Center for Comparative Medicine and Research, The University of Texas MD Anderson Cancer Center (UTMDACC), Bastrop, TX. Experiments were performed in accordance with the Animal Welfare Act and the NIH Guide for the Care and Use of Laboratory Animals. All procedures were performed in accordance to a protocol (00001183-RN00) approved by the Institutional Animal Care and Use Committee at UTMDACC. The implant was assembled as described above with Pt foil electrodes membranes and the reservoir was filled with sterile PBS. Using aseptic technique, a 2 cm skin incision was made in the animal dorsum, mid-thorax parallel

to the spine, approximately 3 cm to the left of the spine. The subcutaneous space was bluntly dissected ventrally to create a pocket for the implant, positioned approximately 2 cm ventral from the incision. The implant was positioned with the circuitry facing the epidermis and membrane facing the dermis. The subcutaneous layer was closed with continuous absorbable monofilament suture (4-0 PDS). The skin was closed in a continuous intradermal pattern with the same suture. Following the minimally invasive implantation of the device, the animal was monitored for any sign of discomfort or unusual behavior. Bluetooth communication with the implanted implant was performed every 5 minutes using the MATLAB® script running on a computer positioned 3 meters away from the animal. Connections to the implant were performed at regular intervals of 1 h for the first 50 h, then every 6 h thereafter. Communication reliability was assessed as in the rats experiment. The implant was explanted after 10 days.

### Histological analysis

Tissues were fixed in 10% neutral-buffered formalin and embedded in paraffin. Five (5  $\mu$ m) slices were cut and stained with hematoxylin & eosin (H&E) at the Research Pathology Core of Houston Methodist Research Institute (HMRI), Houston, TX, USA. Slides were assessed by a pathologist at HMRI.

### Statistical analysis

Graphs were plot and statistical data analysis performed using GraphPad Prism 7 (version 7.0a; GraphPad Software, Inc., La Jolla, CA). Data are represented as mean  $\pm$  SD. Statistical significance was determined using one-way analysis of variance (ANOVA). Release rate for each phase of a cumulative release were considered as the angular coefficient of the first order polynomial fit calculated with MATLAB® polyfit (fitting errors were always under 2%).

## Results and Discussion

The key feature of our platform involves leveraging electric field for modulated control of drug release through nanofluidic membranes. We investigated two types of electrode integration to determine which could offer better performances in terms of drug release modulation via the application of a trans-membrane electric field. In one method, we affixed two platinum (Pt) foils on the top and bottom of the membrane (Figure 1A), while the second method consist of a Pt electrode stack layer sputtered directly onto the membrane surface<sup>27</sup> (Figure 1C).

### Mechanism of drug diffusion in nanofluidic channels

Fluidic behavior at the nanoscale is different from the micro and macroscale<sup>30</sup>. When charged particles diffuse through the nanochannels, they electrostatically interact with the electrical double layer (EDL), which is a counter-ions distribution present at the interface of the charged walls in our silicon nanofluidic membranes. The ratio  $\delta=\lambda/h$  between the Debye length ( $\lambda$ ), a characteristic measure of the extension of the EDL, and the nanochannel size ( $h$ ) represent how much the charged molecule diffusion is influenced by the EDL. When no voltage is applied to the nanofluidic membrane (passive phase), the concentration difference between a high concentration region (drug reservoir) and a low concentration region (sink solution) drives diffusion of the drug molecule through the nanochannels. However, in the passive phase when  $\delta$  is large and the size of molecules approaches  $h$  in order of magnitude, steric and electrostatic hindrance effects imposed by the nanochannels act as a bottleneck for free diffusion, generating a saturated diffusive transport that is quasi-independent from the concentration gradient<sup>31,32</sup>.

In all our experiment the solution used was 50 mM, resulting in a Debye length of  $\lambda = 1.3 \text{ nm}$ . We hypothesized that for small  $\delta$  (i.e.,  $\delta = 0.0065$  for  $h = 200 \text{ nm}$ ) channels with the application of a small trans-membrane electric field (active phase), the active transport of charged molecules would be driven by electrophoresis. In contrast, for larger  $\delta$  (i.e.,  $\delta = 0.1$  for  $h = 13 \text{ nm}$ ) channels which display a charge-selective behavior, we hypothesized that the application of an electric field would generate a redistribution of ionic species at the micro-nanochannel interface. Therefore, we postulated that the active transport of molecules would be affected by ionic depletion and enrichment consistent with the beginning of transition to ionic concentration polarization (ICP).

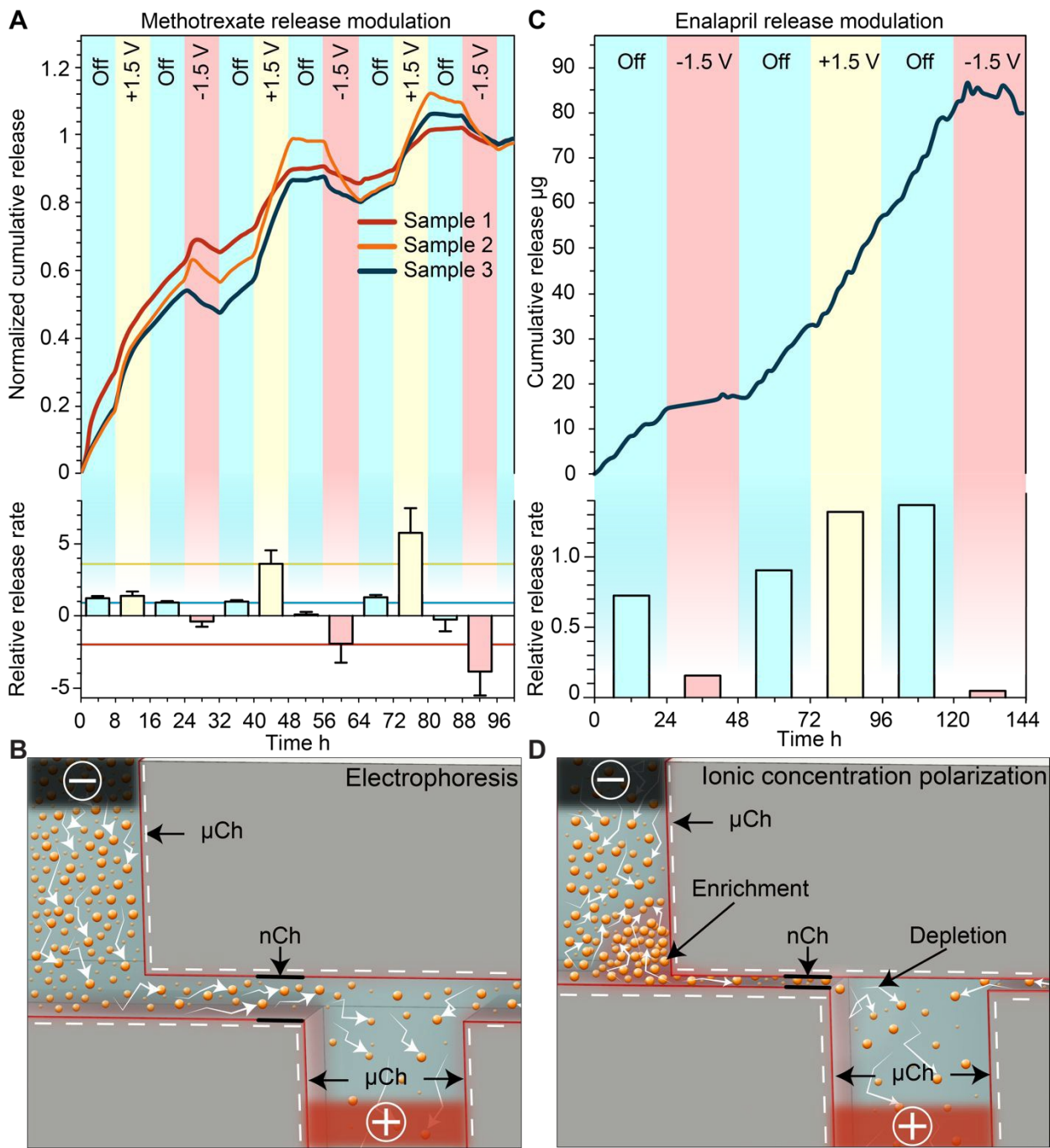


**Figure 2. In vitro release rate of methotrexate and enalapril. (A)** Methotrexate cumulative release (normalized to sink concentration at hour 100) (top) and release rate (bottom) for different applied voltages normalized to its passive release rate. Horizontal lines in the bar plot are the averages of the +1.5 V (yellow), passive (blue) and -1.5 V (red) release rates. Sputtered electrodes configuration employed. **(B)** Schematic of electrophoretic transport in nanochannels. **(C)** Enalapril cumulative release (top) and release rate (bottom) for different applied voltages normalized to its passive release rate. Horizontal lines in the bar plot are the averages of the +1.5 V (yellow), passive (blue) and -1.5 V (red) release rates. Platinum foil electrodes

configuration employed. **(D)** Schematic of ionic concentration polarization in nanochannels, highlighting enrichment and depletion regions.

### **In vitro release modulation of methotrexate**

We first investigated how the application of a low intensity electric field across the membrane with Pt foil electrodes could modify the release rate of methotrexate, an antifolate drug used for first-line treatment of rheumatoid arthritis. For analysis of modulated in vitro release, we alternated between 3 different phases: passive with no applied voltage and two active phases with either negative or positive voltage. Upon application of a +1.5 V potential between the Pt electrodes, a consistent increase of cumulative release rate with respect to the passive phase was observed (Figure 2A). Conversely, the application of -1.5 V resulted in a decrease of release rate compared to the previous phase. Regardless of the polarity of the previously applied potential, upon deactivation of the voltage, the release returned to a zero-order concentration driven diffusion. The release rate calculated for each phase are shown in figure 2A (bottom). To quantify the effect of externally applied potential on the release rate, we averaged the release rate of each phase (horizontal lines) and compared active release to passive release. We observed a 2.5-fold decrease when a negative voltage was applied and a 4.7-fold increase when a positive voltage was applied. When grouping the release rates by phase typology, we detected a statistically significant difference between each group, indicating effective modulation of release rate through the application of the external potential.

The results obtained in this release study, which was performed with a 200 nm membrane, are consistent with electrophoretic charge transport phenomenon (Figure 2B). Specifically, charged molecules in the bulk have a negligible interaction with the EDL and are driven through the channel by the external electric field applied by the electrodes. Additional validation of electrophoretic transport is through the observation of a reduction in methotrexate cumulative release (negative release rate) upon application of a negative voltage. Since our testing setup is a closed system, it is expected that the drug molecule could be driven back into the reservoir if the external electric field overcomes the concentration gradient force. We expect that this phenomenon would not be observed in the subcutaneous space where the drug would be rapidly uptaken by surrounding tissues. These scenarios would instead result in a more pronounced reduction of release rate.

### **In vitro release modulation of enalapril**



To evaluate the drug modulation capability of the electric field across the membrane with sputtered Pt electrodes, we performed an in vitro release study with enalapril. Enalapril is an angiotensin-converting enzyme inhibitor used for management of hypertension. Figure 2C shows the cumulative release achieved with enalapril when cycling through the three different phases. For each passive phase, a quasi-zero-order concentration driven diffusion was achieved with an average of 0.8  $\mu\text{g/h}$  of enalapril released. With the application of a positive voltage, we observed a slight increase in release rate, whereas the application of a negative voltage consistently led to several-fold decrease in release rate. When comparing the release rate of each phase to the passive rate, we observed that a negative applied voltage yielded on average a 7-fold decrease in release rate, while positive applied voltage resulted in a 1.8-fold increase of release rate (Figure C, bottom).

As this study was performed with a smaller membrane (13 nm), the EDL spans over most of the nanochannel volume, which leads to the electrostatic exclusion of co-ions and enrichment of counter-ions (Figure 2D)<sup>33</sup>. When an external tangential electric field is applied, co-ions will start to accumulate in the upstream *enrichment region*, while a *depletion region* will form downstream (Figure 2D). The co-ions enriched region will create both a concentration gradient and an electric field against the externally applied potential, which will prevent additional drug molecules from entering the nanochannels<sup>34</sup>. In fact for enalapril, the application of a negative voltage resulted in a more pronounced decrease in release rate, while a positive voltage yielded a smaller increase in release rate when compared to methotrexate. We attributed this phenomenon to the onset of ICP, which could lead to a reduction in release rate when either a positive or negative potential is applied to the electrodes (Figure 2D).

We have previously demonstrated that in even smaller nanochannels (5.7 nm), ICP can overcome other effects such as electrophoretic force and concentration gradient, leading to a decrease in release rate with either positive or negative applied potentials<sup>35</sup>. Here we observed slightly different passive release rates depending on the previously applied potential, that we attribute to the slow redistribution of ions generated by ICP. This relatively slow ion redistribution allows for a smooth transition of release between different phases. In the eventual need for a sharper transition, the sequence of applied potential can be changed accordingly. Overall, we posit that ICP is an important phenomenon that should be taken into account when modulating the drug release rate through small nanochannels.



### Influence of electrode configuration on drug release modulation

Although the phenomena that lead to release modulation of methotrexate and enalapril differ, we attribute the difference in reproducibility to the employment of different electrode configurations, specifically their relative distance. Pt foil electrodes glued onto the membrane results in a distance of ~1 mm while sputtered electrodes are separated only by the membrane thickness (700  $\mu\text{m}$ ). Our results demonstrated that smaller distance between Pt electrodes yielded a higher intensity of the applied electric field<sup>36</sup> for the same applied potential. In particular we estimated an electric field of 1.5 V/mm and 2.14 V/mm for Pt foil and sputtered electrodes respectively. Therefore, we achieved a more reproducible control of methotrexate release modulation with respect to enalapril.

On the other hand, regardless of the different inter-electrode distance in the two configurations, both electrode integration methods represent feasible approaches to achieve drug modulation via an external electric field. Further considerations for choosing the optimal electrode integration methods concern their fabrication technique. While Pt foils constitute an easier method, they are costly and could prove challenging to adapt to intricate fluidic structures. Conversely, sputter deposition allows for coating of complex surface with a fine control over thickness of the deposited material. However, poor adhesive properties of sputtered Pt to our substrate requires the adoption of other materials such as silicon dioxide ( $\text{SiO}_2$ ) and titanium (Ti) to improve adhesion. Nevertheless, both electrodes are demonstrated to be biocompatible and bioinert<sup>27</sup> and thus suitable for clinical translation.

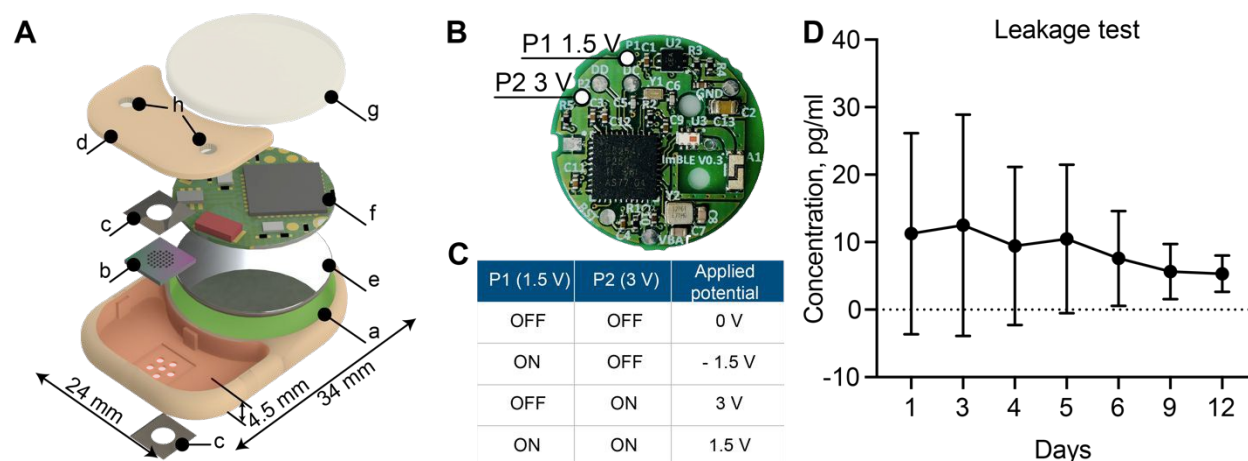


**Figure 3. Implant components, configuration and leakage test.** (A) Exploded view rendering of the implant: a. PEEK body, b. Silicon nanofluidic membrane; c. Platinum foil electrodes; d. PEEK lid used to seal the drug reservoir; e. Battery; f. Printed circuit board (PCB) g. Epoxy sealant; h. Silicone drug filling ports. Red and green highlighted areas are the reservoir compartment and the circuitry chamber,

respectively. **(B)** The printed circuit board (PCB) with the two GPIO output P1 and P2 highlighted, which can apply to the electrodes 1.5 V and 3 V respectively. **(C)** Schematic of possible voltages that can be applied to the membrane. **(D)** Detection of rhodamine B concentration in sink solution over 12 days. Data represented as mean  $\pm$  SD (N=3).

### Remote-controlled implant assembly, working configuration and leakage test

To create an implant which could be brought toward clinical translation, we selected PEEK as the fabrication material. PEEK is commonly used in orthopedic implants due to mechanic robustness and bio-inertness<sup>37</sup>. Importantly, PEEK avoids potential RF-shielding associated with metals such as titanium. The implant hosts two compartments: one for the membrane that also serves as a drug reservoir with 550  $\mu$ l capacity (highlighted in red) and the other for the battery and electronics (highlighted in green) (Figure 3A). The implant dimensions are 34 mm in length, 24 mm in width and 4.5 mm in thickness for a total volume of 2.8 cm<sup>3</sup>. The reservoir occupies 20% of the implant volume, while circuitry chamber accounts for 40%. Notably, by comparing our implant to a relevant existing implant technology (Microchip), our implant hosts a drug reservoir  $\sim$ 200 times larger, while maintaining an overall volume 5 times smaller than Microchip<sup>20</sup>. This larger reservoir capacity could minimize excessive surgical procedures for implant replacement, which is a current challenge with existing implants of similar functions<sup>20</sup>. An alternative to increasing reservoir capacity is through integration of refilling ports for drug replenishment, as previously demonstrated by our group<sup>38</sup>.

In order to achieve different drug release rates, a different combination of P1 and P2 *ON* and *OFF* status on the PCB allows for the application of 4 different voltages, +1.5 V, -1.5 V, +3 V and 0 V (Figure 3B). As summarized in figure 3C, when both P1 and P2 are *ON*, the applied voltage to the electrodes is +1.5 V; when P1 is *ON* and P2 is *OFF*, the applied voltage is -1.5 V; when P1 is *OFF* and P2 is *ON*, the applied voltage is +3 V; and when P1 and P2 are both *OFF*, the applied voltage is 0 V.

To ensure implant intactness and impermeability, we performed a leakage test with rhodamine B, a fluorescent dye used as a surrogate marker. The cumulative concentration of rhodamine B presented in figure 3D showed no significant change in concentration over the 12 days of analysis, confirming implant intactness. We attributed the higher dye concentration observed initially to residual dye deposited on the outside of the implant during the loading procedure. At the end of the study, after syringe withdrawal of residual dye from the reservoir via the port, we examined

the implant internally for permeability assessment. All internal components remained dry, confirming implant intactness and impermeability.

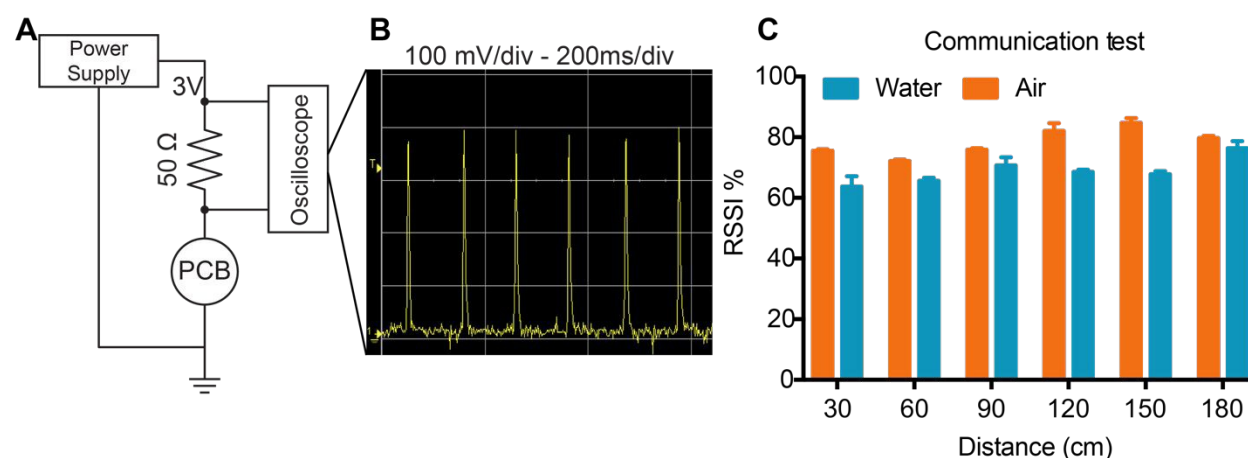


**Figure 4. Power consumption and communication stability.** (A) Experimental setup for the PCB power consumption test. (B) Oscilloscope measurements representing the amount of power request from the circuitry to advertise its presence via Bluetooth Low Energy. All the other PCB activity are completely obscured by the advertising phases. (C) Communication stability test, in open air vs water container. Data represented as mean  $\pm$  SD (N=15).

### Power consumption analysis

To estimate the lifespan of our implantable device, we assessed the different sources of power consumption of the PCB (Figure 4A). Circuitry activity can be divided into background use, advertising and communication. Background processing and advertising (peaks in Figure 4B) consumed 97.5  $\mu$ W and 16.5  $\mu$ W, respectively. Data transmission during a connection between implant and server resulted in significant energy consuming activity spending 1.22 mW. Further, the current flow between the two electrodes for drug modulation also account for battery depletion. Specifically, current measurements during enalapril and methotrexate in vitro release study (Figure 2) ranged from a few  $\mu$ A to peaks of 100  $\mu$ A (150  $\mu$ W). In view of the contribution of these sources of battery drainage (capacity of 270 mWh), we estimated the lifetime of the implant in a high power consumption scenario to reach 20 days (Supplementary Information).

We used different approaches to extend the lifetime of our implant. By reducing the advertising frequency from 100 ms to 10 s, the calculated lifespan was extended to 30 days without a considerable loss in connection stability. Similarly, in order to reduce energy used by the electrodes, a possible solution is to investigate the application of a square or pulse wave with a

duty cycle set in agreement with the characteristic response time of the system. A hypothetical reduction of current consumption to 1  $\mu$ A, could extend the implant lifespan to 3 months. Another approach to decrease power consumption is to reduce connections, for example exchanging the current state of the implant in a secure code via advertising (Supplementary Information). In our current setting, the constant exchange of parameters represents a security measure, in order to avoid unexpected actions. For our current implant, this could translate to an extended lifespan of several months.

**In vitro communication stability analysis**

To verify proper RF-communications we performed a communication test, where a connection was initiated between the remote control and the implant. The results showed that with the increase of the distance between the implant and the receiver, there is no definite drop of signal power up to 180 cm. In fact, the transmission power in air has an RSSI that is almost consistently 80% for all distances tested. In water, the RSSI is approximately 70% at every distance. In order to ensure a stable connection, signal quality should be above 25-30%. Here we observed a signal quality above 60% for both in air and in water for every distance ensuring stable connections up to 180 cm with ample margin.

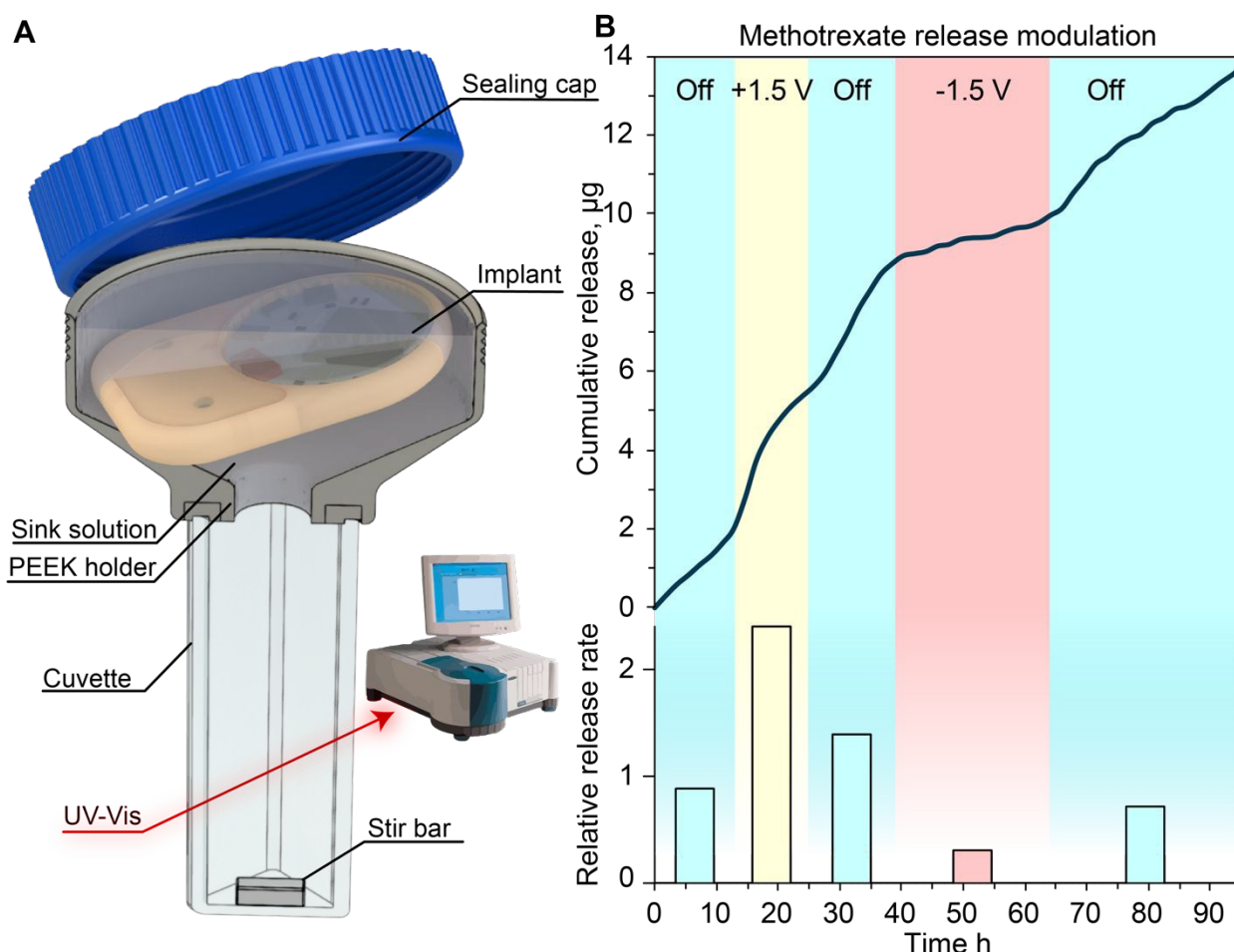


**Figure 5. In vitro release of methotrexate with assembled implant. (A)** Experimental setup for the in vitro release. The implant is in a sealed cuvette, phases are set by remote communication with the nearby computer. Drug concentration in the sink solution is measured via UV-Vis (Cary 50 Bio represented). **(B)** Methotrexate cumulative release (top) and release rate (bottom) for every applied voltage normalized to the passive release rate.

### In vitro modulated release analysis with assembled nanofluidic implant

To assess the drug release modulation capability of the fully assembled implant, we performed an in vitro release study of methotrexate. The implant was positioned in a custom-made cuvette as depicted in Figure 5A. The release rate and duration of each phase was controlled by the MATLAB® script running on a nearby computer. By sending a Bluetooth command to the immersed implant on a predetermined schedule, the script executed the application of an electric field across the nanochannels. This communication allowed the alternation of passive phases that resulted in a purely diffusive transport, with active phases that leveraged nano-electrofluidic transport to alter the release rate. Depending on the polarity of the generated electric field, an

increase or decrease of release rate was obtained (Figure 5B). Upon deactivation of the applied potential after the active phases, the release reverted to zero-order concentration-driven diffusion. When comparing the release rate of each phase to the average of the passive phase (Figure 5B, bottom), we observed that the application of +1.5 V lead to a 2.4-fold increase of methotrexate release resulting in a release rate of 9.3  $\mu\text{g/day}$ . Conversely the application of -1.5 V resulted in a 3.24-fold decrease and a release rate of 1.2  $\mu\text{g/day}$ . A similar dosage of methotrexate injected subcutaneously was demonstrated to be effective in treating rats without side effects <sup>39</sup>.

Throughout this experiment, we achieved a reliable signal strength up to 3 meters with no communications errors and smooth transition between different release rates. The slight delay observed in the onset of a different release rate was attributed to the testing apparatus and the time that it takes for the stir bar to homogenize the sink solution concentration<sup>29</sup>. Our results with the nanofluidic implant demonstrated fine control in timing and dose administration which could be tailored to the individual's specific pathology.

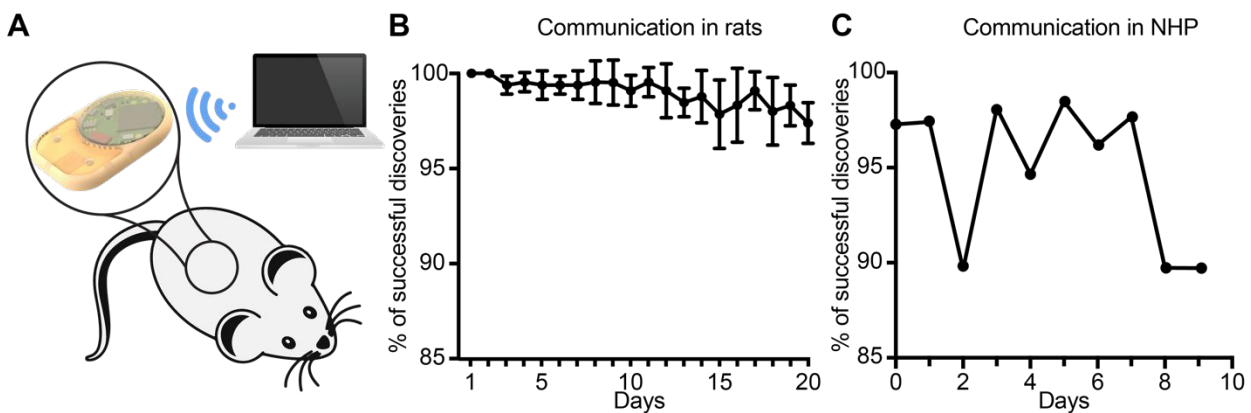


**Figure 6. Communication reliability in rats and non human primate.** (A) Custom MATLAB® script for the remote control of several implants at the same time. (B) Percentage of the successful discovery of implants (n=6) subcutaneously implanted in rats. Data shows mean  $\pm$  SD. (C) Daily successful discoveries of the implant in non human primate.

**In vivo remote communication assessment in rats and non human primate**

To validate the reliability of remote communication with our implant, we performed in vivo experiments in rats and in a non-human primate (NHP), in view of future clinical translational goals. Communication reliability was assessed by quantifying lost advertisement packets during the discovery routine of the MATLAB® script (Figure 6A). In rats, the percentage of successful implant discovery was relatively stable for up to 11 days and thereafter showed a decreasing trend that



we attributed to the slow discharging of the battery (Figure 6B). In the NHP, we observed an average of ~95% successful discoveries over 9 days (Figure 6C).

It is important to note that a missing discovery does not represent an error in communication, but loss of advertisement packets. In the case of rats, battery discharging prevented brief but substantial burst of energy required for wireless communication, resulting in reduced power to the antenna, and consequently a shorter communication range. In NHP, we ascribed loss of advertisement packets to the considerable distance between the implant and external antenna due to the large confinement area of the animal. Therefore, a plausible solution is to employ a longer discovery interval in the server. Despite the loss of some packets during the advertisement phase, all the connections established were successful. In fact, the security routine that provides a feedback control loop and ensures that the read status is the same as the implemented was never triggered.

Remote connection via BLE offers high versatility allowing our implanted devices to interact in real-time with external servers, such as smartphones, smartwatches, or computers. We chose a completely automated MATLAB® script to perform all experiments since it obviates the need for operator intervention, which could be particularly useful in future clinical deployments. Additionally, we developed two other communication systems: an iOS application (Supplementary Fig. 1) and a web application that allows real-time monitoring of all active implants (Supplementary Fig. 2). These applications can be used as a patient monitoring method for physicians to remotely check or change release regimen of the implanted devices. Remote communication and control can reduce recurring clinic visits, improve patient adherence and therapeutic effectiveness and set the pace for the future of telemedicine and patient care.

### **In vivo biocompatibility in rats and non human primates**

For preclinical safety assessment of our implant, we evaluated biocompatibility in rats as well as NHP. NHPs provide high biological relevance especially in the context of immunotoxic side effects. In rats, throughout the duration of the 21-day study, the implants were well tolerated with no observed adverse skin reactions, infection or variation in their social behavior and mobility. Upon explantation, we observed fibrous encapsulation of the implant, indicative of foreign body reaction conventional to medical implants<sup>40,41</sup>. Histological analysis was performed on the fibrotic capsule adjacent to the Pt electrode (Figure 7A), epoxy (Figure 7B) and PEEK (Figure 7C). The side of the capsule facing the three aforementioned materials showed resolved mild inflammation



and the presence of collagen, consistent with fibrosis formation. In particular, in areas near the Pt electrode and epoxy, minimal macrophage infiltration was detected. In areas near the PEEK material, we observed presence of a minimal inflammation region in the final healing stages. Overall, there were no signs of significant active inflammatory reaction after 21 days of implantation, suggesting biocompatibility and tolerability of our implant.

In NHP, X-ray imaging performed after the implantation surgery demonstrated implant positioning with visible circuitry chamber and Pt electrodes (Figure 7D). Histological assessment of tissue adjacent to the epoxy (Figure 7E) and PEEK (Figure 7F) side of the implant both showed an ongoing inflammation characterized by the presence of leukocytes and macrophages. Based on typical foreign body response, we posit that the inflammation observed is transient and associated with the recent surgical procedure for implantation of the device. Moreover, the acute inflammatory reaction observed was possibly augmented due to the young age of the animal, which typically have a robust immune system. Nonetheless, we observed regions with initial development of fibrous tissue, indicative of transition into the last phase of the foreign body response.

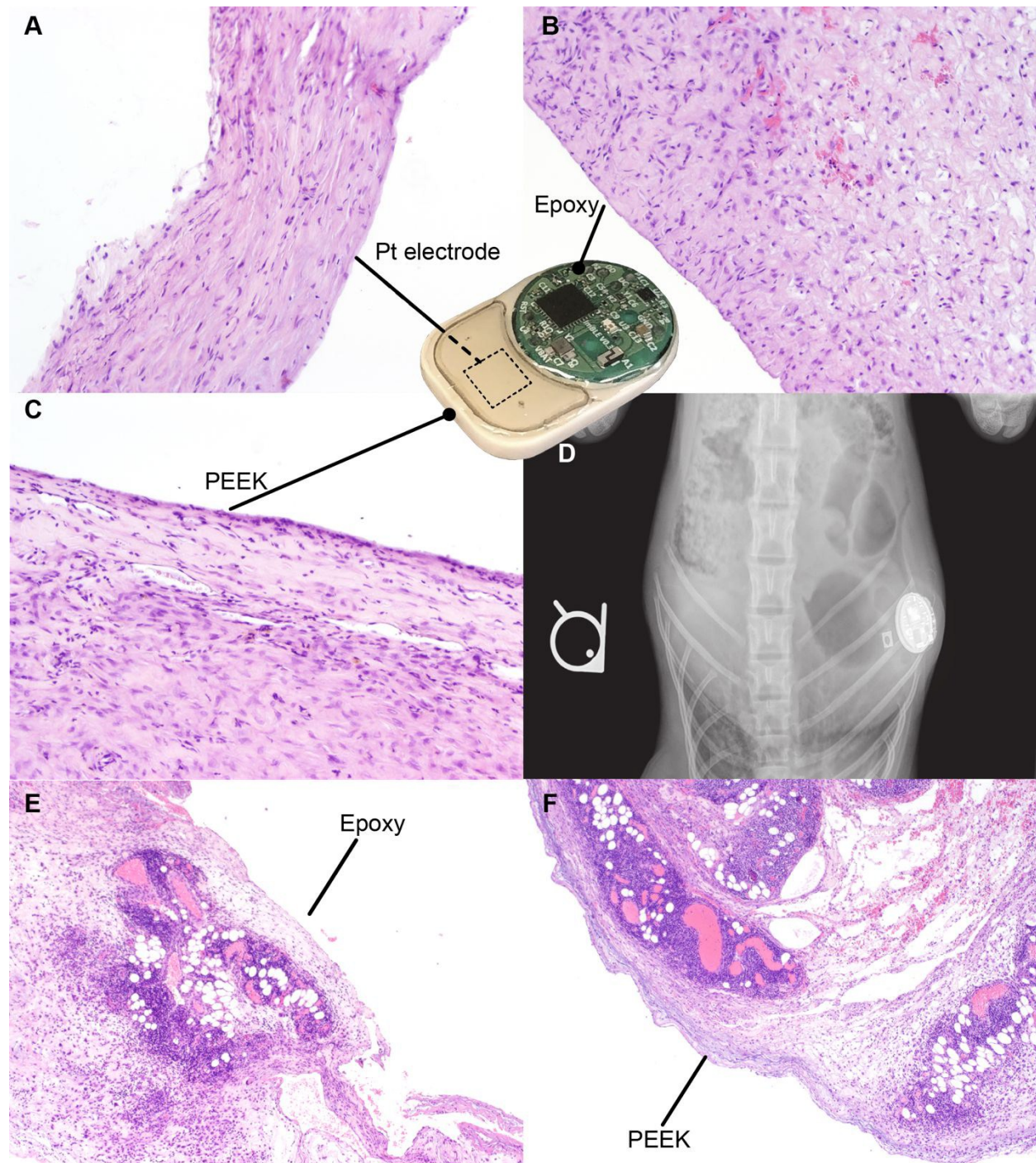


**Figure 7. Biocompatibility test in rats and non human primate.** Histology of the fibrotic capsule in contact with platinum electrode (A), epoxy (B) and PEEK (C) in rats. (D) Post-surgery X-ray image of implant to assess implant positioning. Histology of the surrounding tissue adjacent to the PEEK (B) and epoxy (C) sides of the implant in non human primate.

## Conclusion and future outlook

Here we presented a proof of concept study of a remotely controlled implantable device that leverages electric field induced nanofluidic phenomena for tunable drug delivery. Our ongoing investigations are dedicated to minimization of power consumption for extended implant lifespan. With a sufficiently longer implant lifespan, we could extend release duration of each phase to better evaluate in vivo controlled drug delivery performances. Currently in vivo drug concentration measurements of the different release phases could be easily confounded by drug pharmacokinetic tail, normal physiological fluctuation, or inherent animal to animal variability.

While we anticipate that technological innovations of high-energy density batteries could soon be helpful, we are exploring alternative ways to control the applied electric field. In particular we are investigating the application of a gate potential to modulate the EDL in the nanochannels as a mean to modify the release of drugs. With the development of a properly isolated gate electrode, electrostatic gating could in fact offer extremely low power consumption<sup>34,42,43</sup>.

Although further developments are needed, this proof of concept study sets the foundation for a generation of nanofluidic implants for tunable drug delivery. The ability to control and remotely administer therapy offers a feasible approach for precision medicine, chronotherapy or telemedicine purposes. More than that, remote-controlled drug delivery could increase patient compliance, in scenarios where conventional administration is painful or inconvenient, specifically for children, elderly or disabled individuals. Moreover, the potential of our technology resides in its versatility, in which numerous types of drugs can be released, allowing for treatment for a vast spectrum of pathologies. Future development could entail integration with other implantable sensors that could trigger drug release creating a close-feedback-loop to achieve desired therapy.

**Author contribution**

- NDT: conceptualization, data curation, formal analysis, investigation, software, visualization, writing – original draft
- AS: formal analysis, visualization, writing – original draft
- GB: conceptualization, data curation, investigation, software
- TG: conceptualization, data curation, investigation
- CYXC: validation, writing – original draft
- AprilG: investigation
- GR: investigation

CSF: conceptualization, formal analysis

DD: conceptualization

AlessandroG: conceptualization, funding acquisition, project administration, validation

## Conflict of interest

All authors declare no conflict of interest.

## Acknowledgements

Membranes were provided by NanoMedical Systems. Funding support from the Houston Methodist Research Institute, NIH R21GM111544, NIH-NIGMS R01GM127558.

## References

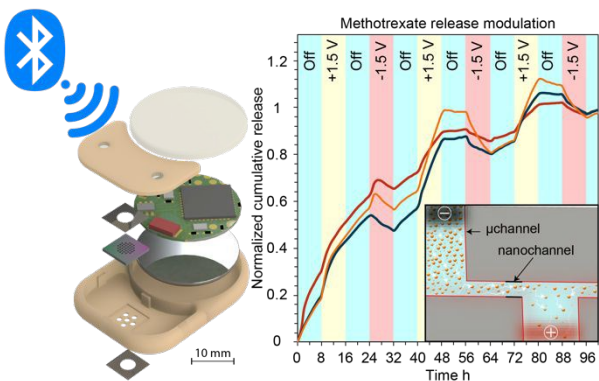
- 1 I. Poureslami, L. Nimmon, I. Rootman and M. J. Fitzgerald, *Health Promot. Int.*, 2016, **32**, 743–754.
- 2 W. Raghupathi and V. Raghupathi, *Int. J. Environ. Res. Public. Health*, 2018, **15**, 431.
- 3 R. Reynolds, S. Dennis, I. Hasan, J. Slewa, W. Chen, D. Tian, S. Bobba and N. Zwar, *BMC Fam. Pract.*, 2018, **19**, 11.
- 4 L. Peeples, *Nature*, 2018, **556**, 290–292.
- 5 A. Kumar and J. Pillai, in *Nanostructures for the Engineering of Cells, Tissues and Organs*, ed. A. M. Grumezescu, William Andrew Publishing, 2018, pp. 473–511.
- 6 G. Tiwari, R. Tiwari, B. Sriwastawa, L. Bhati, S. Pandey, P. Pandey and S. K. Bannerjee, *Int. J. Pharm. Investig.*, 2012, **2**, 2–11.
- 7 F. C. Bartter, C. S. Delea, W. Baker, F. Halberg and J. K. Lee, *Chronobiologia*, 1976, **3**, 199–213.
- 8 S.-Y. Lin and Y. Kawashima, *J. Controlled Release*, 2012, **157**, 331–353.
- 9 G. Kaur, C. Phillips, K. Wong and B. Saini, *Int. J. Clin. Pharm.*, 2013, **35**, 344–358.
- 10 F. Lévi, *Lancet Oncol.*, 2001, **2**, 307–315.
- 11 F. P. Pons-Faudoa, A. Ballerini, J. Sakamoto and A. Grattoni, *Biomed. Microdevices*, 2019, **21**, 47.
- 12 A. Santos, M. S. Aw, M. Bariana, T. Kumeria, Y. Wang and D. Losic, *J. Mater. Chem. B*, 2014, **2**, 6157–6182.
- 13 L. Claes and A. Ignatius, *Chir.*, 2002, **73**, 990–996.
- 14 H. Tian, Z. Tang, X. Zhuang, X. Chen and X. Jing, *Prog. Polym. Sci.*, 2012, **37**, 237–280.
- 15 G. V. Gill, D. J. Husband, P. D. Wright, G. Sharpe, R. Taylor, S. Walford, S. M. Marshall and K. G. Alberti, *Diabetes Res.*, 1986, **3**, 135–137.
- 16 B. Yue, R. Brendel, A. Lukitsch, T. Prentice and B. Doty, *Neuromodulation Technol. Neural Interface*, 2017, **20**, 397–404.



- 17A. Michael, E. Buffen, R. Rauck, W. Anderson, M. McGirt and H. V. Mendenhall, *Pain Med.*, 2012, **13**, 175–184.
- 18B. P. Timko, M. Arruebo, S. A. Shankarappa, J. B. McAlvin, O. S. Okonkwo, B. Mizrahi, C. F. Stefanescu, L. Gomez, J. Zhu, A. Zhu, J. Santamaria, R. Langer and D. S. Kohane, *Proc. Natl. Acad. Sci.*, 2014, **111**, 1349–1354.
- 19T. Hoare, B. P. Timko, J. Santamaria, G. F. Goya, S. Irusta, S. Lau, C. F. Stefanescu, D. Lin, R. Langer and D. S. Kohane, *Nano Lett.*, 2011, **11**, 1395–1400.
- 20J. T. Santini, M. J. Cima and R. Langer, *Nature*, 1999, **397**, 335–338.
- 21M. Staples, K. Daniel, M. J. Cima and R. Langer, *Pharm. Res.*, 2006, **23**, 847–863.
- 22R. Farra, N. F. Sheppard, L. McCabe, R. M. Neer, J. M. Anderson, J. T. Santini, M. J. Cima and R. Langer, *Sci. Transl. Med.*, 2012, **4**, 122ra21–122ra21.
- 23J. J. Sheehan, K. R. Reilly, D.-J. Fu and L. Alphs, *Innov. Clin. Neurosci.*, 2012, **9**, 17–23.
- 24A. Ahmad and W. R. Garnett, *Clin. Drug Investig.*, 2005, **25**, 669–673.
- 25D. Fine, A. Grattoni, S. Hosali, A. Ziemys, E. D. Rosa, J. Gill, R. Medema, L. Hudson, M. Kojic, M. Milosevic, L. B. Iii, R. Goodall, M. Ferrari and X. Liu, *Lab. Chip*, 2010, **10**, 3074–3083.
- 26C. Coletti, M. J. Jaroszeski, A. Pallaoro, A. M. Hoff, S. Iannotta and S. E. Sadow, *Conf. Proc. Annu. Int. Conf. IEEE Eng. Med. Biol. Soc. IEEE Eng. Med. Biol. Soc. Annu. Conf.*, 2007, **2007**, 5850–5853.
- 27T. Geninatti, G. Bruno, B. Barile, R. L. Hood, M. Farina, J. Schmulen, G. Canavese and A. Grattoni, *Biomed. Microdevices*, 2015, **17**, 24.
- 28A. Grattoni, D. Fine, E. Zabre, A. Ziemys, J. Gill, Y. Mackeyev, M. A. Cheney, D. C. Danila, S. Hosali, L. J. Wilson, F. Hussain and M. Ferrari, *ACS Nano*, 2011, **5**, 9382–9391.
- 29T. Geninatti, E. Small and A. Grattoni, *Meas. Sci. Technol.*, 2014, **25**, 027003.
- 30R. B. Schoch, J. Han and P. Renaud, *Rev. Mod. Phys.*, 2008, **80**, 839–883.
- 31G. Bruno, N. Di Trani, R. L. Hood, E. Zabre, C. S. Filgueira, G. Canavese, P. Jain, Z. Smith, D. Demarchi, S. Hosali, A. Pimpinelli, M. Ferrari and A. Grattoni, *Nat. Commun.*, , DOI:10.1038/s41467-018-04133-8.
- 32N. Di Trani, P. Jain, C. Y. X. Chua, J. S. Ho, G. Bruno, A. Susnjar, F. P. Pons-Faudoa, A. Sizovs, R. L. Hood, Z. W. Smith, A. Ballerini, C. S. Filgueira and A. Grattoni, *Nanomedicine Nanotechnol. Biol. Med.*, 2019, **16**, 1–9.
- 33A. Plecis, R. B. Schoch and P. Renaud, *Nano Lett.*, 2005, **5**, 1147–1155.
- 34S. Kim, E. I. Ozalp, M. Darwish and J. A. Weldon, *Nanoscale*, 2018, **10**, 20740–20747.
- 35G. Bruno, T. Geninatti, R. L. Hood, D. Fine, G. Scorrano, J. Schmulen, S. Hosali, M. Ferrari and A. Grattoni, *Nanoscale*, 2015, **7**, 5240–5248.
- 36Y. Eckstein, G. Yossifon, A. Seifert and T. Miloh, *J. Colloid Interface Sci.*, 2009, **338**, 243–249.
- 37S. M. Kurtz and J. N. Devine, *Biomaterials*, 2007, **28**, 4845–4869.
- 38C. Y. X. Chua, P. Jain, A. Susnjar, J. Rhudy, M. Folci, A. Ballerini, A. Gilbert, S. Singh, G. Bruno, C. S. Filgueira, C. Yee, E. B. Butler and A. Grattoni, *J. Controlled Release*, 2018, **285**, 23–34.
- 39D.-Y. Liu, H.-K. Lon, Y.-L. Wang, D. C. DuBois, R. R. Almon and W. J. Jusko, *Biopharm. Drug Dispos.*, 2013, **34**, 203–214.
- 40J. M. Anderson, A. Rodriguez and D. T. Chang, *Semin. Immunol.*, 2008, **20**, 86–100.
- 41M. Kastellorizios, N. Tipnis and D. J. Burgess, in *Immune Responses to Biosurfaces*, eds. J. D. Lambris, K. N. Ekdahl, D. Ricklin and B. Nilsson, Springer International Publishing, Cham, 2015, vol. 865, pp. 93–108.

- 42 G. Bruno, G. Canavese, X. Liu, C. S. Filgueira, A. Sacco, D. Demarchi, M. Ferrari and A. Grattoni, *Nanoscale*, 2016, **8**, 18718–18725.
- 43 D. Fine, A. Grattoni, E. Zabre, F. Hussein, M. Ferrari and X. Liu, *Lab. Chip*, 2011, **11**, 2526.

Table of content



Implantable nanofluidic device for remote controlled drug delivery.